Aviation Turbulence Induced by the Interaction between a Jet Stream and Deep Convection

Haoming Chen[1], Xiaoming Shi[1], Christy Yan Yu Leung[2], Ping Cheung[2], Pak Wai Chan[2]

[1]Division of Environment and Sustainability, Hong Kong University of Science and Technology, Hong Kong, China
[2]Hong Kong Observatory, Hong Kong, China

Key Points:

- A regionally convection-permitting model and a new eddy dissipation rate calculation method were used to predict aviation turbulence.
- Deep convection acted like terrain and interacted with a jet stream, causing an upper-level windstorm downstream of the convection top.
- Severe turbulence upstream and downstream of convection was due to different mechanisms, but both related to Kelvin-Helmholtz instability.

Corresponding author: Xiaoming Shi, `shixm@ust.hk`

Abstract

On December 18, 2022, Hawaiian Airlines flight HA35 encountered severe turbulence in a cloud-free region without warning. We simulated this incident using the Model for Prediction Across Scales (MPAS) with a convective permitting grid. We found that the turbulence formed due to the Kelvin-Helmholtz instability (KHI) generated by strong vertical wind shear. At low altitudes, deep convection caused a decrease in wind speed in both upstream and downstream regions. At upper levels, the jet descended and accelerated after flowing over the convection, which acted like a barrier and produced a situation similar to a downslope windstorm. The low Scorer parameter above the jet and the self-induced critical level created the locally enhanced descending jet stream, which destabilized the flow through KHI.

Plain Language Summary

On December 18, 2022, Hawaiian Airlines flight HA35 encountered severe turbulence without warning, resulting in injuries to some passengers and damage to the equipment. This unusual incident requires careful investigation to broaden our understanding of aviation turbulence. A numerical model at kilometer-scale resolution was used to simulate this case and reveal the dynamics, and we successfully captured the occurrence of turbulence with the simulation. The cause of the turbulence was a previously unknown mechanism. It involves the interaction between the deep convection that acted as a barrier and an upper-level jet. Severe turbulence was generated in a situation similar to a downslope windstorm near the ground due to mountains. This interaction caused turbulence in different locations near the strong convection, making the turbulence unpredictable because it occurs in cloud-free regions and cannot be detected by airborne radar.

1 Introduction

The turbulence in aviation is a significant contributor to weather-related incidents, causing injuries, occasional fatalities, and structural damage annually. Furthermore, it incurs considerable operational expenses for airlines, resulting in schedule disruptions and air traffic management challenges, amounting to millions of dollars (Tvaryanas, 2003; R. D. Sharman, Doyle, & Shapiro, 2012; Kim & Chun, 2016; R. Sharman & Lane, 2016a). Aviation turbulence is classified according to its sources: convection-induced turbulence (CIT), mountain wave turbulence (MWT), and clear-air turbulence, which are always generated by atmospheric instabilities, such as static, Kelvin–Helmholtz (KHI), convectively, conditional instabilities(R. Sharman & Lane, 2016b). Specifically, turbulence motions can be active in convection and its surrounding air because of moist instability. They can be generated by the strong deformation of the flow near the cloud and gravity wave breaking (Lane et al., 2003; Trier et al., 2012).

Topography can also induce turbulence because of the formation of gravity waves over the lee side of the mountain when flow passes the terrain. The significant amplitude and fragmentation of these waves induce turbulence. This phenomenon depends on the characteristics of the upstream environment, terrain geometry, and atmospheric stability at different altitudes (Clark & Peltier, 1984; R. Sharman & Lane, 2016b). At high altitudes, the "critical layers" where the wind reverses direction with height are important (R. D. Sharman, Trier, et al., 2012); at low altitudes, the possible "hydraulic jump" can make the flow turbulent (Prósper et al., 2019). Hydraulic jump derives from hydraulics and is a phenomenon that the thickness of a flow is rapidly increased. It usually occurs when a high-velocity fluid enters a low-velocity region, where the thickness of the fluid rises due to the opposite relationship between the thickness and energy of the supercritical and subcritical flow. Previous researchers have primarily examined the effects of MWT at high altitudes, as it is the altitude range that directly impacts aircraft.

However, what will happen if this terrain is suspended in the air? Fujita (1982) found that deep convection can act like a topographical feature (virtual terrain), inducing the upstream flow to either deflect or go over it. Under appropriate atmospheric conditions and convection, it can even generate a hydraulic jump at high altitudes, resulting in turbulence downwind (O'Neill et al., 2021). Our research reveals that strong convection functions as a topographical feature, inducing high-altitude jet streams to generate turbulence in distinct regions downstream of the convection. This mechanism differs from previous studies focused on CIT though this region has strong convection. Furthermore, the velocity of the jet increase as they descend, leading us to believe that this process is similar to the formation mechanism of a downslope windstorm.

Downslope windstorms have been observed in mountainous regions worldwide (Fudeyasu et al., 2008; Koletsis et al., 2009) and relevant studies utilized various methodologies such as observation and numerical simulations (Doyle & Smith, 2003; Klemp & Lilly, 1975), which showed the nonlinear effects on large-amplitude mountain waves. To explain these nonlinear effects, various theories have been developed: 1) the flow undergoes a transition from subcritical flow upstream to supercritical flow downstream (D. R. Durran, 1986; Smith, 1985; Long, 1953); 2) the upward propagating waves are reflected downward by an area where the Scrorer parameter changes rapidly, which creates a superposition of the wave to increase the wind velocity (Klemp & Lilly, 1975); and 3) the "self-induced critical layer" can trap the energy to increase the wave amplitude (Peltier & Clark, 1979; Clark & Peltier, 1984).

In this research, we used the Model for Prediction Across Scales (MPAS) to study a case of severe aviation turbulence that happened near the Hawaiian Islands. The accident left 25 people injured, some seriously, and the condition of "smooth with clear skies" (Oxenden, 2023) suggests its complex mechanisms involved. MPAS has the flexibility and advantage to cover global circulation but refine its grid mesh to a convection-permitting resolution regionally. It is found that the server turbulence is caused by a new mechanism not considered before in aviation turbulence, which is due to the interaction between the jet stream and deep convection.

2 Models and Methods

2.1 MPAS Setup

The MPAS version 7 is used in this study for regionally convection-permitting simulations. It is characterized by a non-hydrostatic dynamical core using unstructured Voronoi meshes and C-grid discretization (Skamarock et al., 2012). The global variable-resolution mesh can have finer resolutions in interested areas. This study focuses on aviation turbulence near Hawaii Islands. Our experiments are designed with $1 \sim 60$, $3 \sim 60$ and $9 \sim 60$ km meshes. Figure S1 in supplementary materials shows the mesh configurations, which have higher resolution near the Hawaiian Islands and offshore waters and gradually change to 60-km resolution in the background. The analysis is the results from the $1 \sim 60$ mesh if not specified otherwise. Different resolutions help to test the sensitivity of the simulated convection and turbulence to grid spacings.

The initial conditions are based on the European Centre for Medium-Range Weather Forecast (ECMWF) fifth-generation reanalysis (ERA5) data at a 0.25° horizontal grid spacing and 37 vertical levels (Bell et al., 2021). The initialization time of our simulations is approximately 6 hours before the occurrence of the incident. The MPAS has a vertical profile consisting of 55 layers, with the highest layer situated at an altitude of 22 km above the surface. The experiments turned off the convection parameterization since switching it off can usually provide a higher intensity of turbulence. We used the MPAS microphysics suite, which uses the Thompson scheme (Thompson et al., 2008) for grid cells smaller than 10 km and the WSM6 scheme (Hong et al., 2006) for other cells,

the planetary boundary layer scheme suite, which uses the YSU (Hong, 2010) at the courser resolution and the MYNN (Nakanishi & Niino, 2009) at the finer resolution. The Noah land surface scheme (F. Chen & Dudhia, 2001), and the RRTMG short and longwave radiation schemes (Mlawer et al., 1997; Iacono et al., 2000) are used in all simulations.

2.2 Calculation of Eddy Dissipation Rate (EDR)

A new method to estimate EDR based on convection-permitting model output and subfilter-scale reconstruction has been developed by H. Chen et al. (2023). It has been proven to be more effective in capturing turbulence than other methods. This method separates subfilter scales into resolvable subfilter scales (RSFS) and subgrid scales (SGS). The RSFS components have much more energy than the SGS component. Thus, we compute the RSFS part only. Following (Chow et al., 2005). The reconstructed RSFS velocity

$$\widetilde{u}_i^* = \overline{\widetilde{u}}_i + (I-G)\overline{\widetilde{u}}_i + (I-G)(I-G)\overline{\widetilde{u}}_i + \cdots \tag{1}$$

where the overline denotes the filter, the tilde denotes discretization, $\overline{\widetilde{u}}_i$ is, therefore, the grid variable from MPAS, I is the identity operator, and G is the filter. In this study, the filter is a top-hat filter applied to all three dimensions. Keeping $\overline{\widetilde{u}}_i$ is the zero-order reconstruction and is what we adopted. Including more terms on the right side of Eq. 1 generates higher-order reconstruction, which is not used in this study because it may occasionally generate negative TKE.

After obtaining RSFS velocities, the RSFS TKE is

$$\mathrm{TKE} = \frac{1}{2}\left(\overline{\widetilde{u}_i^*\widetilde{u}_i^*} - \overline{\widetilde{u}}_i^*\overline{\widetilde{u}}_i^*\right) \tag{2}$$

And assuming the turbulence is in the inertial subrange, the EDR is the following (Schumann, 1991),

$$\varepsilon^{1/3} = \left(\mathrm{TKE}^{3/2}/L\right)^{1/3} \tag{3}$$

where $L = (\lambda\Delta x\Delta y\Delta z)^{1/3}$ is the integral scale of the turbulence, Δx, Δy and Δz are grid spacings. In our calculations, we interpolated MPAS data from the unstructured grid to $0.008^\circ\times0.008^\circ$ latitude-longitude grid before using the above equations. Therefore, Δx and Δy are approximately 0.8 km for the region near Hawaii Islands. Δz is 500 m. $\lambda = 8$ for our calculation. However, in principle, one could adjust this factor λ to calibrate EDR estimation for the operational forecast.

2.3 Other Physical Quantities

The Froude number (Fr) in this case was calculated from

$$\mathrm{Fr} = \frac{U}{NH} \tag{4}$$

here, the U is the velocity of the upstream wind, N is the Brunt–Vaisala frequency, and H is the height of flow descent (O'Neill et al., 2021), and we extracted the flow by some specific isentropes, it will be described later, so the U and N is the average in the flow. If $\mathrm{Fr} \gg 1$, the flow passes over the barrier with small changes(Carruthers & Hunt, 1990), if $\mathrm{Fr} \ll 1$, the flow will be blocked and have substantial nonlinear effects(Smolarkiewicz & Rotunno, 1989), and the $\mathrm{Fr} \sim 1$ means transitional flow may happen.

The Scorer parameter l^2, an value to evaluate if a gravity wave can propagate through a region, is defined as follows:

$$l^2 = \frac{N^2}{U^2} - \frac{1}{U}\frac{d^2U}{dz^2} \tag{5}$$

Waves with horizontal wave numbers larger than l^2 are evanescent(D. Durran, 2003).

3 Results

3.1 Environmental Conditions

Figure 1 a) shows a map of the large-scale wind field, geopotential height and the brightness temperature from GOES-17(?, ?) at 200 hPa on December 18, 2022, 20:10 UTC. It exhibits extensive cloud coverage over the western Hawaiian Islands and over the sea to the northeast. The clouds are located in the exit region of a distorted mid-latitude jet stream, due to a low pressure in the northwest of Hawaii. Notably, the clouds' altitude is relatively low, and the airplane was traversing a cloud-free region. The wind near Hawaii is southwesterly, opposite to the direction of the aircraft's flight path.

The horizontal distributions of the total hydrometeors at altitudes of 5200 m and 10200 m are presented in Figure 1 b) and c), showing the consistency with observation, wherein the aircraft track is represented by a red line. The airplane's trajectory was located in a region with less convection around its path, but it was still affected by strong turbulence. Notably, the lower altitudes exhibit more convective activity, and some alerts about thunderstorms in the vicinity were raised. At high altitudes, convection is reduced, with sporadic strong convection forming a loosely organized arc perpendicular to the prevailing wind direction.

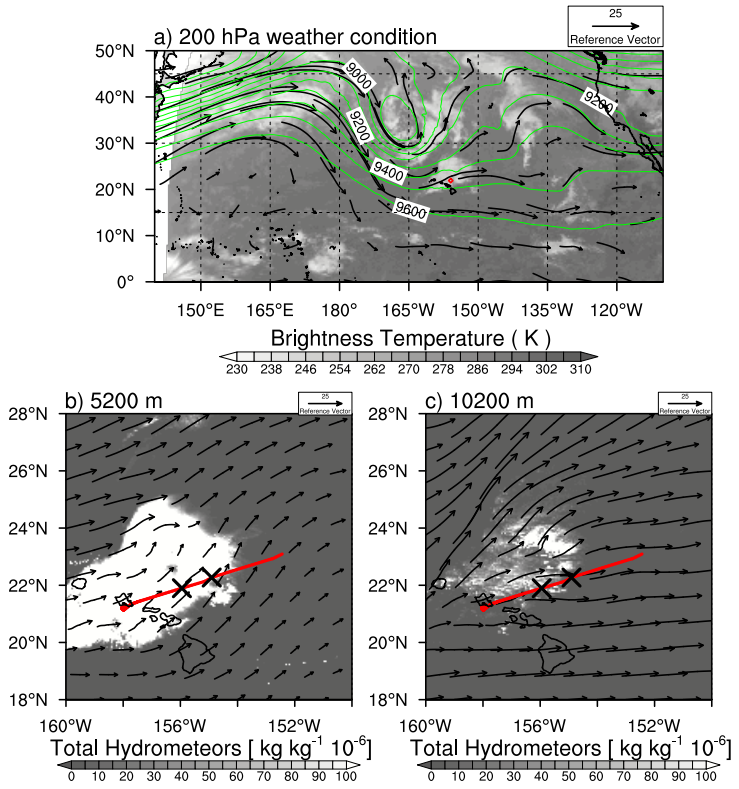

Figure 1. a) Horizontal distribution of brightness temperature (shading) from GOES-17, 200-hPa wind (vectors), and geopotential height (unit: m, green contour). b) total hydrometeors in MPAS simulation at 5200 m, c) sas as (b) but at 10200 m. These data are on December 18, 2022, at 20:10 UTC. The red square in (a) indicates the location of aviation turbulence events. The red lines in (b) and (c) represent the airplane's path. The two crosses mark the positions of turbulence events

Additional figures about wind at different altitudes can be found in Figure S2 in the supplementary material. It can be found that there exists a low-speed region to the northwest of the airplane path, southwest of the convection, and the positions of convection can be indicated in Supplementary Figure S3 with vertical velocity. This suggests the influence of the convection system on the wind field, as evidenced by an increase in speed over the convection.

3.2 Validation of Simulations

Based on media coverage and flight data, we know there were two approximate locations where the turbulence happened. Figure 2 shows the distribution of EDR on the cross-section along the airplane's trajectory from different simulations at 20:10 UTC on December 18, 2022. The red line represents the aircraft's path, while the two markers denote the locations where turbulence incidents occurred. The lower marker, situated at an altitude of 11 km, corresponds to the trajectory at 20:16 UTC. The higher marker, positioned at an altitude of 12.5 km, corresponds to the trajectory at 20:08 UTC. In the aircraft's trajectory record, a rapid 500 ft descent was observed near this upper-level incident, followed by a return to the original altitude.

In Figure 2, the x-coordinate denotes distance. The moderate and severe intensity turbulence (EDR ≥ 0.22) has a descending distribution at altitudes exceeding 12 km, with the wake just intersecting the flight track. At the altitude of 10 km, the turbulence displays a stable, mostly horizontal distribution, with a thickness of approximately 1 km within the x-range of 0 to 450 km, beyond which the altitude of the turbulent layer decreases to $8 \sim 10$ km. Notably, the turbulence occupies a high altitude but is confined to a narrow horizontal distance around $x = 350$ km. There was a series of deep convective systems in that area, serving as the source of this turbulence. Overall, the pattern of turbulence remains qualitatively consistent at different resolutions. Similar distributions can be seen in ERA5 data, but there are some location discrepancies, and the deep convection is missing. In two turbulence incident locations, all three MPAS simulations show EDR values significantly higher in surrounding regions. The higher resolution produced higher values. These resolution-depending results are consistent with our previous resolution testing results and previous research(Barber et al., 2018).

Notably, the resolution dependency cannot be fixed by a simple adjustment with a constant scaling factor. For example, if the 9-km resolution results are doubled to reach the magnitude of 1-km resolution simulation results, it will overestimate the turbulence in 6 $\sim$10 km height range, x coordinate $100 \sim 300$ km. Additionally, when observing the coordinates of convective clusters, which are areas where turbulence appears in a column shape, the 1-km resolution results are further to the east, indicating a delay in the development of convection in the low-resolution results. Therefore, the higher resolution appears to be necessary for simulations.

Figure 2 e), f) shows the distributions of the EDR in different altitudes at 20:10 UTC on December 18, 2022, from the 1-km resolution simulation. The southern red lines represent the flight path of the airplane. We found that, especially at high altitudes, the eastern incident location is actually part of a large turbulence area. The wind speed map (Fig. 1) also shows a low wind speed area to the northwest of the aircraft's path, followed by wind vectors pointing to a large area with intense turbulence. Therefore, in order to better reveal the mechanism of turbulence, we can examine the section along the green line, which is to the north of the flight trajectory.

3.3 Turbulence Generation Mechanisms

Figure 3 shows the cross-section (green line in Fig. 2) for different turbulence indices overlaid by EDR contours for regions with EDR higher than 0.25. We marked three

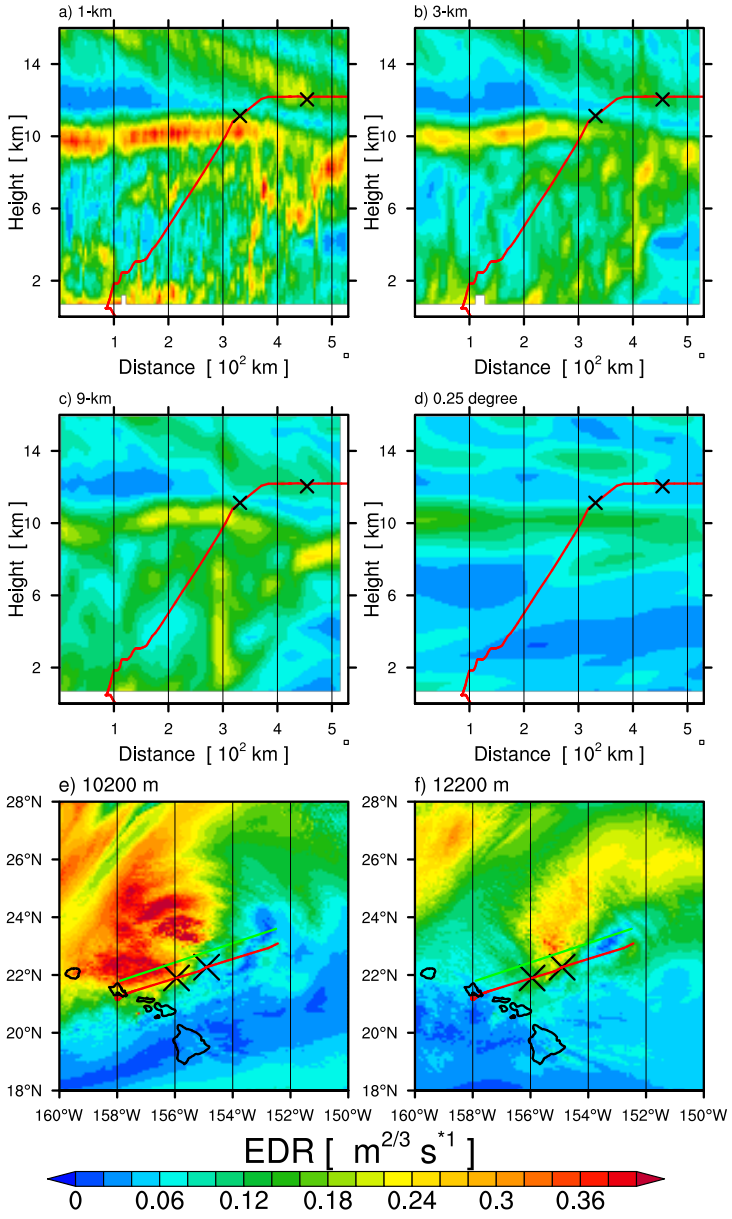

Figure 2. Cross sections along the path of the airplane, with the distribution of EDR from different resolutions a) 1 km, b) 3 km, c) 9 km and d) 0.25° and horizontal distribution of the EDR from 1- km mesh with different altitudes. e) 10200 m, f) 12200 m. at December 18, 2022, 20:10 UTC, while the ERA5 result is on December 18, 2022, 20:00 UTC. The red line represents the path of the airplane, the two notations represent the positions of turbulence events. The green line represents the new section.

regions, with each part exhibiting moderate or high-intensity turbulence. The first two regions encompass the areas below the jet and on both the upstream and downstream sides of the convection, respectively. The third section pertains to the region above the descending jet.

By comparing the indices for turbulence based on wind shear and other different mechanisms, we found that all turbulence in the three marked regions appears to be generated by the KHI, which is mainly driven by strong vertical wind shear. From Figure 3 a) and b), strong vertical wind shear, low Richardson number, and high EDR regions tend to overlap. In Figure 3 c), the Ellrod index is greater than 25 over many areas, which would be considered as severe turbulence (Ellrod & Knapp, 1992), but Region 3 is not covered at all. In Figure 3 d), the regions where sign changes of potential vorticity (PV) exist are considered to have turbulence (Audrey et al., 2011). The PV sign changes mainly occur in the vicinity of convection, and this PV-based prediction is very inaccurate regarding the location of turbulence.

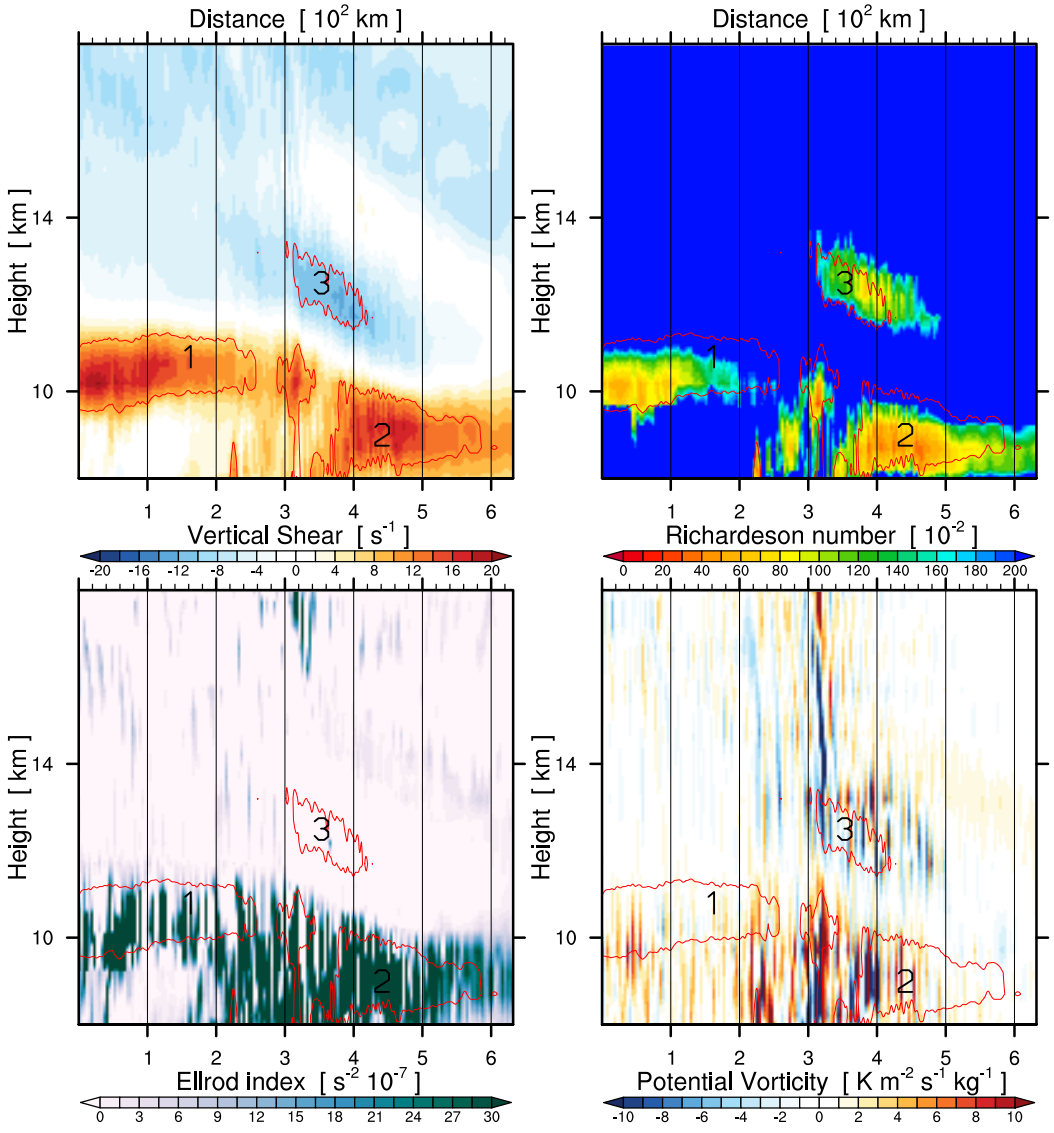

Figure 3. Vertical cross-sections of a) wind shear, b) Richardson number, c) Ellrod index, and d) potential vorticity on December 18, 2022, at 20:10 UTC. The area where EDR is higher than 0.25 is highlighted with the red contour in all panels. The numbers in the figure mark different turbulent regions.

In Regions 1 and 2. The hindering effect of convection caused low-speed areas upstream and downstream and combined with the jet at 11 km altitude, resulting in stronger wind shear below the jet, leading to KHI.

The Region 3 appears to be unique because of the relatively low-speed air. It occurs above the jet descent region, which results from the interaction between deep convection and the preexisting jet. The turbulence in this region originates from a situation similar to a low-level downslope windstorm due to mountains. We will discuss the details of the flow structure and mechanisms in the next section.

3.4 Windstorm Over Deep Convection

This section concentrates on how the high-altitude jet and convection interact to yield flow acceleration when the jet flows over the convection, as well as the structure of this 'downslope' jet.

Figure 4 shows cross-sections of simulated potential temperature, wind, vertical motions, and the Scorer parameter at 20:00, 20:20, and 20:40 UTC on December 18, 2022. This figure reveals the location of the convection through the presence of strong vertical velocity, which exhibits slow movement. The height of hydrometeors drops significantly after crossing the strong convection. Concurrently, the altitude where the jet acceleration occurs, as well as the turbulent region, follow the development and movement of the convective system with time. Notably, at 20:20, the convective activity intensifies at x coordinate of 240 km, causing the isentropes above to be warped upwards. These flow characteristics suggest that the strong convection acted as a barrier to the jet stream.

Figure 4 indicates that below the altitude of 11 km and before reaching the x-coordinate of 250 km, the wind vector exhibits an upward lift. There is a large positive area of vertical velocities, which signifies the occurrence of an upward process of the flow to the western region of the convection and shows the topography-like effects from deep convection. Meanwhile, the jet maintains a relatively stable height. Upon flowing over the convective system, the isentropes with a height between $10 \sim 14$ km undergo a significant drop in height, decreasing by 1.5 km in height within a horizontal range of approximately 180 km. Moreover, the wind speed undergoes a notable increase during the descent at the downstream side of the convection, with the average wind speed rising from 40 to 50 m/s, indicating the presence of a downslope storm-like high-speed region. At half of the descent height, the isentropes adopt a wavy pattern with a short wavelength of approximately $7 \sim 8$ km.

Some theories used to explain downslope windstorms require a critical layer. In resonant amplification theory, it is typically thought to isolate the effect of gravity waves that propagate vertically, which may be induced by a directional shift in wind or strong vertical shear. An area of a lower Scorer parameter or the lower Richardson number can also lead to this effect. In the theory of transitional flow, since the Fr needs to be calculated based on Equation 4, the obstacle's height is important.

In our investigation, the high-altitude jet is a component of large-scale circulation and is not ubiquitous across the entirety of high-altitude regions in middle latitudes. Consequently, the vertical wind shear is substantial in the layers immediately above and below the jet, as evidenced by Figure 4 j), k) and l). Additionally, a lower Scorer parameter is present at an altitude range of $12 \sim 14$ km and $8.5 \sim 10$ km prior to crossing the convection.

Therefore, a well-functioning waveguide has been generated before traversing the convection. Upon crossing the convection, the gravity waves are stimulated and reflected back towards the jet from the low Scorer parameter region. It results in an increase in the velocity of the jet due to the resonance as well as the wind shear, which leads to a

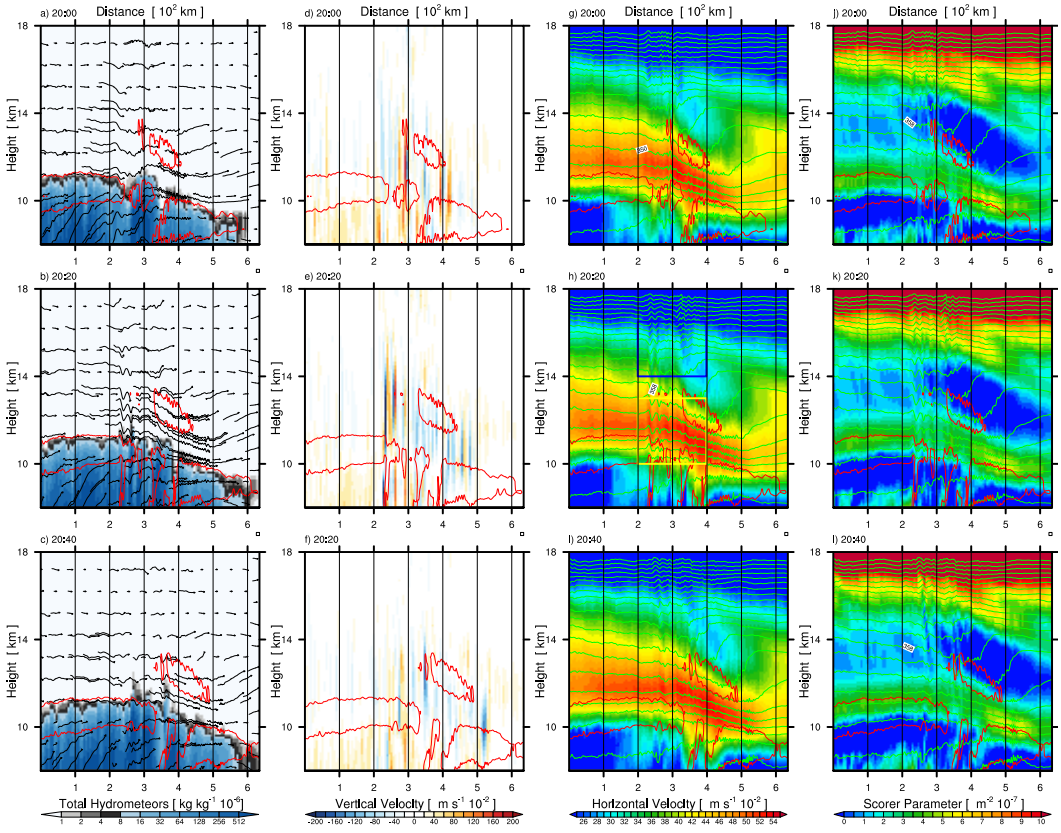

Figure 4. Cross-sections of different variables (columns). The rows represent different times on December 18, 2022, at 20:00, 20:20, and 20:40 UTC. a), b) and c) show total hydrometeors; d), e) and f) show the vertical velocity, g), h) and i) are the horizontal wind speed along the section; and j), k) and l) are the Scorer parameter. Wind vectors reference the orientation of the cross-section and are superimposed on a), b), and c). Potential temperature is superimposed as green contours with an interval of 4 K. The area where EDR is higher than 0.25 is highlighted with the red contour in all panels. shades)

lower scorer parameter at the higher altitude of the jet so that the wave can break here more easily; it can be recognized as the self-induced critical level. Thus, a positive feedback system is established. In Figure 4 g), h) and i), there is an area of low-speed wind between altitude 12.5 $\sim$ 14 km, x coordinate 350 $\sim$ 480 km, where overturning and breaking of the gravity wave is pronounced.

In an alternative hydraulics theory of transition flow, a critical level is still important, but we can find the representations of flows directly, isentropes in the blue box in Figure 4 h) exhibit a pattern of initial descent followed by an ascent downstream of the convection. This behaviour is consistent with a subcritical flow. A supercritical flow behaves in the opposite way. In the yellow box, the isentropes exhibit a consistent descent. This trend is indicative of transition flow, where the flow undergoes acceleration before and after crossing the convection since the state of the flow is converted to supercritical flow.

In this theory, it is necessary to calculate the Fr to determine the state of the flow. It is very complex to calculate this number for this virtual terrain. Though the deep convection can act as the terrain from previous analysis, it can constantly evolve, and its

barrier effects vary at different times and locations, and some air parcels may penetrate the deep convection directly. Nonetheless, we tentatively separate the jet from the background by extracting the area from the potential temperature between 338 K and 350 K, since they envelop the core of the jet and the isentropes, depicting the characteristics of the transitional flow. By applying the Equation 4, and the H here can be set as 1500 m by comparing the same isentropes downstream, we obtain the Fr is 1.08 at 20:10, and this value indicates a transitional flow can happen. The condition is favourable for downslope windstorms and a hydraulic jump.

4 Conclusions

In this study, we used the MPAS that utilizes a regionally convection-permitting mesh to simulate a severe aviation turbulence incident near the Hawaiian Islands. This model is capable of accurately simulating both the large-scale and local wind fields. Additionally, we applied a recently developed subfilter-scale reconstruction method to estimate EDR from the convection-permitting model output. Our findings confirm this approach is effective in predicting aviation turbulence.

In this case, the airplane experienced severe turbulence abruptly in the cloud-free region without any alerts. The environment has convection mostly at lower altitudes, with very few convective cells occurring above 8000 m. As the airplane typically cruises at around 12,000 m, relying solely on cloud distribution for warning would assume a smooth flight process. However, in this case, we find that the turbulence originated from the interaction between the large-scale jet and local deep convection, causing the turbulence to develop extensively and strongly outside the clouds.

The weather conditions of this case created a situation similar to downslope windstorms caused by terrain. Deep convection played the role of 'terrain' in the air, and the movement of the turbulent area following the convective system confirmed this effect. The jet stream, brought to low latitudes by a low-pressure system, has an exit region near Hawaii. It created the region of a low Scorer parameter immediately above and below the jet. After passing over the convection, barrier-caused gravity waves broke on the downstream side of the convection top and created a wave-induced critical level, which overlaid with the previously mentioned low Scorer parameter region, amplifying the reflection of gravity waves and causing the jet to accelerate during its descent. The presence of continuous descending isentropes during the process and the critical value of the Fr also suggest the existence of transitional flow. The jet streams created low Richardson number regions, which favour the generation of severe turbulence. This interaction between mid-latitude jet streams and deep convection is a new mechanism of aviation turbulence not appreciated before. Our case study provides insights to prevent the encounter of aviation turbulence in cloud-free regions.

Open Research Section

The ERA5 hourly data in different levels(Bell et al., 2021) can be downloaded on `https://cds.climate.copernicus.eu/cdsapp#!/dataset/10.24381/cds.bd0915c6?tab=overview`. The flight data can be downloaded from `https://www.flightradar24.com/data/flights/ha35` (membership required). The GOES-17(GOES-R Series Program, 2019) satellite data can be downloaded from `https://www.avl.class.noaa.gov/saa/products/welcome`.

Acknowledgments

The project is part of the Aviation Research and Development Project Phase 2 (AvRDP2), supported by World Meteorological Organization. The authors thank HKUST Fok Ying

Tung Research Institute and National Supercomputing Center in Guangzhou Nansha sub-center for providing high performance computational resources.

References

Audrey, C., Christine, L., Yves, B., & Francois, B. (2011, December). Aeronautical diagnostics for Clear-Air Turbulence forecast at Meteofrance in the context of DELICAT European project. *Journal of Physics: Conference Series*, *318*(7), 072007. doi: 10.1088/1742-6596/318/7/072007

Barber, K. A., Mullendore, G. L., & Alexander, M. J. (2018, January). Out-of-Cloud Convective Turbulence: Estimation Method and Impacts of Model Resolution. *Journal of Applied Meteorology and Climatology*, *57*(1), 121–136. doi: 10.1175/JAMC-D-17-0174.1

Bell, B., Hersbach, H., Simmons, A., Berrisford, P., Dahlgren, P., Horányi, A., ... Thépaut, J.-N. (2021). The ERA5 global reanalysis: Preliminary extension to 1950. *Quarterly Journal of the Royal Meteorological Society*, *147*(741), 4186–4227. doi: 10.1002/qj.4174

Carruthers, D. J., & Hunt, J. C. R. (1990). Fluid Mechanics of Airflow over Hills: Turbulence, Fluxes, and Waves in the Boundary Layer. In *Atmospheric Processes over Complex Terrain* (pp. 83–107). Boston, MA: American Meteorological Society. doi: 10.1007/978-1-935704-25-6_5

Chen, F., & Dudhia, J. (2001, April). Coupling an Advanced Land Surface–Hydrology Model with the Penn State–NCAR MM5 Modeling System. Part I: Model Implementation and Sensitivity. *Monthly Weather Review*, *129*(4), 569–585. doi: 10.1175/1520-0493(2001)129⟨0569:CAALSH⟩2.0.CO;2

Chen, H., Liu, H., Leung, C. Y.-Y., Cheung, P., Chan, S. T., & Shi, X. (2023, July). Predicting convection-induced turbulencewith regionally convection-permitting simulations. *Monthly Weather Review*, Submitted.

Chow, F. K., Street, R. L., Xue, M., & Ferziger, J. H. (2005, July). Explicit Filtering and Reconstruction Turbulence Modeling for Large-Eddy Simulation of Neutral Boundary Layer Flow. *Journal of the Atmospheric Sciences*, *62*(7), 2058–2077. doi: 10.1175/JAS3456.1

Clark, T. L., & Peltier, W. R. (1984, November). Critical Level Reflection and the Resonant Growth of Nonlinear Mountain Waves. *Journal of the Atmospheric Sciences*, *41*(21), 3122–3134. doi: 10.1175/1520-0469(1984)041⟨3122:CLRATR⟩2.0.CO;2

Doyle, J. D., & Smith, R. B. (2003). Mountain waves over the Hohe Tauern: Influence of upstream diabatic effects. *Quarterly Journal of the Royal Meteorological Society*, *129*(588), 799–823. doi: 10.1256/qj.01.205

Durran, D. (2003). LEE WAVES AND MOUNTAIN WAVES. In *Encyclopedia of Atmospheric Sciences* (pp. 1161–1169). Elsevier. doi: 10.1016/B0-12-227090-8/00202-5

Durran, D. R. (1986, November). Another Look at Downslope Windstorms. Part I: The Development of Analogs to Supercritical Flow in an Infinitely Deep, Continuously Stratified Fluid. *Journal of the Atmospheric Sciences*, *43*(21), 2527–2543. doi: 10.1175/1520-0469(1986)043⟨2527:ALADWP⟩2.0.CO;2

Ellrod, G. P., & Knapp, D. I. (1992, March). An Objective Clear-Air Turbulence Forecasting Technique: Verification and Operational Use. *Weather and Forecasting*, *7*(1), 150–165. doi: 10.1175/1520-0434(1992)007⟨0150:AOCATF⟩2.0.CO;2

Fudeyasu, H., Kuwagata, T., Ohashi, Y., Suzuki, S.-i., Kiyohara, Y., & Hozumi, Y. (2008, January). Numerical Study of the Local Downslope Wind "Hirodo-Kaze" in Japan. *Monthly Weather Review*, *136*(1), 27–40. doi: 10.1175/2007MWR2049.1

Fujita, T. T. (1982). Principle of Stereoscopic Height Computations and their Appli-

cations to Stratospheric Cirrus over Severe Thunderstorms. *Journal of the Meteorological Society of Japan. Ser. II*, *60*(1), 355–368. doi: 10.2151/jmsj1965.60.1_355

GOES-R Series Program. (2019). *NOAA GOES-R Series Advanced Baseline Imager (ABI) Level 0 Data.* NOAA National Centers for Environmental Information. doi: 10.25921/TVWS-W071

Hong, S.-Y. (2010, July). A new stable boundary-layer mixing scheme and its impact on the simulated East Asian summer monsoon. *Quarterly Journal of the Royal Meteorological Society*, *136*(651), 1481–1496. doi: 10.1002/qj.665

Hong, S.-Y., Kim, J.-h., Lim, J.-o., & Dudhia, J. (2006, March). The WRF single moment microphysics scheme (WSM). *Journal of the Korean Meteorological Society*, *42*, 129–151.

Iacono, M. J., Mlawer, E. J., Clough, S. A., & Morcrette, J.-J. (2000, June). Impact of an improved longwave radiation model, RRTM, on the energy budget and thermodynamic properties of the NCAR community climate model, CCM3. *Journal of Geophysical Research: Atmospheres*, *105*(D11), 14873–14890. doi: 10.1029/2000JD900091

Kim, S.-H., & Chun, H.-Y. (2016, October). Aviation turbulence encounters detected from aircraft observations: Spatiotemporal characteristics and application to Korean Aviation Turbulence Guidance: Aviation turbulence encounters detected from aircraft observations. *Meteorological Applications*, *23*(4), 594–604. doi: 10.1002/met.1581

Klemp, J. B., & Lilly, D. R. (1975, February). The Dynamics of Wave-Induced Downslope Winds. *Journal of the Atmospheric Sciences*, *32*(2), 320–339. doi: 10.1175/1520-0469(1975)032⟨0320:TDOWID⟩2.0.CO;2

Koletsis, I., Lagouvardos, K., Kotroni, V., & Bartzokas, A. (2009, October). Numerical study of a downslope windstorm in Northwestern Greece. *Atmospheric Research*, *94*(2), 178–193. doi: 10.1016/j.atmosres.2009.05.012

Lane, T. P., Sharman, R. D., Clark, T. L., & Hsu, H.-M. (2003, May). An Investigation of Turbulence Generation Mechanisms above Deep Convection. *Journal of the Atmospheric Sciences*, *60*(10), 1297–1321. doi: 10.1175/1520-0469(2003)60⟨1297:AIOTGM⟩2.0.CO;2

Long, R. R. (1953, February). Some Aspects of the Flow of Stratified Fluids: I. A Theoretical Investigation. *Tellus*, *5*(1), 42–58. doi: 10.1111/j.2153-3490.1953.tb01035.x

Mlawer, E. J., Taubman, S. J., Brown, P. D., Iacono, M. J., & Clough, S. A. (1997, July). Radiative transfer for inhomogeneous atmospheres: RRTM, a validated correlated-k model for the longwave. *Journal of Geophysical Research: Atmospheres*, *102*(D14), 16663–16682. doi: 10.1029/97JD00237

Nakanishi, M., & Niino, H. (2009). Development of an Improved Turbulence Closure Model for the Atmospheric Boundary Layer. *Journal of the Meteorological Society of Japan. Ser. II*, *87*(5), 895–912. doi: 10.2151/jmsj.87.895

O'Neill, M. E., Orf, L., Heymsfield, G. M., & Halbert, K. (2021, September). Hydraulic jump dynamics above supercell thunderstorms. *Science (New York, N.Y.)*, *373*(6560), 1248–1251. doi: 10.1126/science.abh3857

Oxenden, M. (2023, January). Cloud 'Shot Up' Just Before Severe Turbulence Struck, Report Says. *The New York Times*.

Peltier, W. R., & Clark, T. L. (1979, August). The Evolution and Stability of Finite-Amplitude Mountain Waves. Part II: Surface Wave Drag and Severe Downslope Windstorms. *Journal of the Atmospheric Sciences*, *36*(8), 1498–1529. doi: 10.1175/1520-0469(1979)036⟨1498:TEASOF⟩2.0.CO;2

Prósper, M. A., Sosa Tinoco, I., Otero-Casal, C., & Miguez-Macho, G. (2019, July). Downslope windstorms in the Isthmus of Tehuantepec during Tehuantepecer events: A numerical study with WRF high-resolution simulations. *Earth System Dynamics*, *10*(3), 485–499. doi: 10.5194/esd-10-485-2019

Schumann, U. (1991, August). Subgrid length-scales for large-eddy simulation of stratified turbulence. *Theoretical and Computational Fluid Dynamics*, *2*(5), 279–290. doi: 10.1007/BF00271468

Sharman, R., & Lane, T. (Eds.). (2016a). *Aviation Turbulence*. Cham: Springer International Publishing. doi: 10.1007/978-3-319-23630-8

Sharman, R., & Lane, T. (Eds.). (2016b). *Aviation Turbulence*. Cham: Springer International Publishing. doi: 10.1007/978-3-319-23630-8

Sharman, R. D., Doyle, J. D., & Shapiro, M. A. (2012, January). An Investigation of a Commercial Aircraft Encounter with Severe Clear-Air Turbulence over Western Greenland. *Journal of Applied Meteorology and Climatology*, *51*(1), 42–53. doi: 10.1175/JAMC-D-11-044.1

Sharman, R. D., Trier, S. B., Lane, T. P., & Doyle, J. D. (2012, June). Sources and dynamics of turbulence in the upper troposphere and lower stratosphere: A review: FRONTIER. *Geophysical Research Letters*, *39*(12), n/a-n/a. doi: 10.1029/2012GL051996

Skamarock, W. C., Klemp, J. B., Duda, M. G., Fowler, L. D., Park, S.-H., & Ringler, T. D. (2012, September). A Multiscale Nonhydrostatic Atmospheric Model Using Centroidal Voronoi Tesselations and C-Grid Staggering. *Monthly Weather Review*, *140*(9), 3090–3105. doi: 10.1175/MWR-D-11-00215.1

Smith, R. B. (1985, December). On Severe Downslope Winds. *Journal of the Atmospheric Sciences*, *42*(23), 2597–2603. doi: 10.1175/1520-0469(1985)042⟨2597:OSDW⟩2.0.CO;2

Smolarkiewicz, P. K., & Rotunno, R. (1989, April). Low Froude Number Flow Past Three-Dimensional Obstacles. Part I: Baroclinically Generated Lee Vortices. *Journal of the Atmospheric Sciences*, *46*(8), 1154–1164. doi: 10.1175/1520-0469(1989)046⟨1154:LFNFPT⟩2.0.CO;2

Thompson, G., Field, P. R., Rasmussen, R. M., & Hall, W. D. (2008, December). Explicit Forecasts of Winter Precipitation Using an Improved Bulk Microphysics Scheme. Part II: Implementation of a New Snow Parameterization. *Monthly Weather Review*, *136*(12), 5095–5115. doi: 10.1175/2008MWR2387.1

Trier, S. B., Sharman, R. D., & Lane, T. P. (2012, August). Influences of Moist Convection on a Cold-Season Outbreak of Clear-Air Turbulence (CAT). *Monthly Weather Review*, *140*(8), 2477–2496. doi: 10.1175/MWR-D-11-00353.1

Tvaryanas, A. P. (2003, September). Epidemiology of Turbulence-Related Injuries in Airline Cabin Crew, 1992–2001. *Aviation, Space, and Environmental Medicine*, *74*(9), 970–976.

Figure 1.

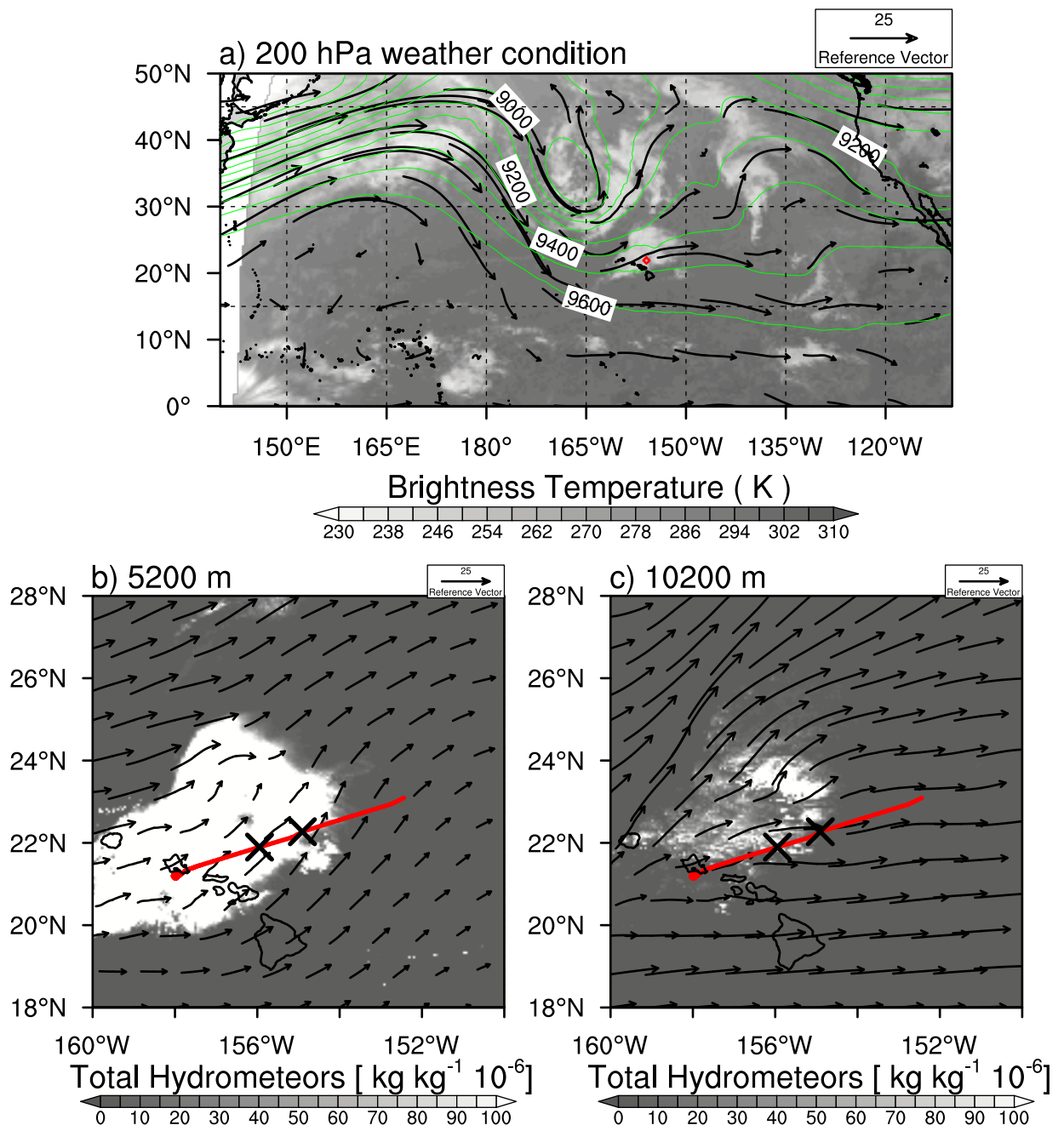
a) 200 hPa weather condition
25
Reference Vector
50°N
40°N
30°N
20°N
10°N
0°
9000
9200
9400
9600
9200
150°E
165°E
180°
165°W
150°W
135°W
120°W
Brightness Temperature (K)
230 238 246 254 262 270 278 286 294 302 310
b) 5200 m
25
Reference Vector
28°N
26°N
24°N
22°N
20°N
18°N
160°W
156°W
152°W
Total Hydrometeors [kg kg-1 10-6]
0 10 20 30 40 50 60 70 80 90 100
c) 10200 m
25
Reference Vector
28°N
26°N
24°N
22°N
20°N
18°N
160°W
156°W
152°W
Total Hydrometeors [kg kg-1 10-6]
0 10 20 30 40 50 60 70 80 90 100

Figure 2.

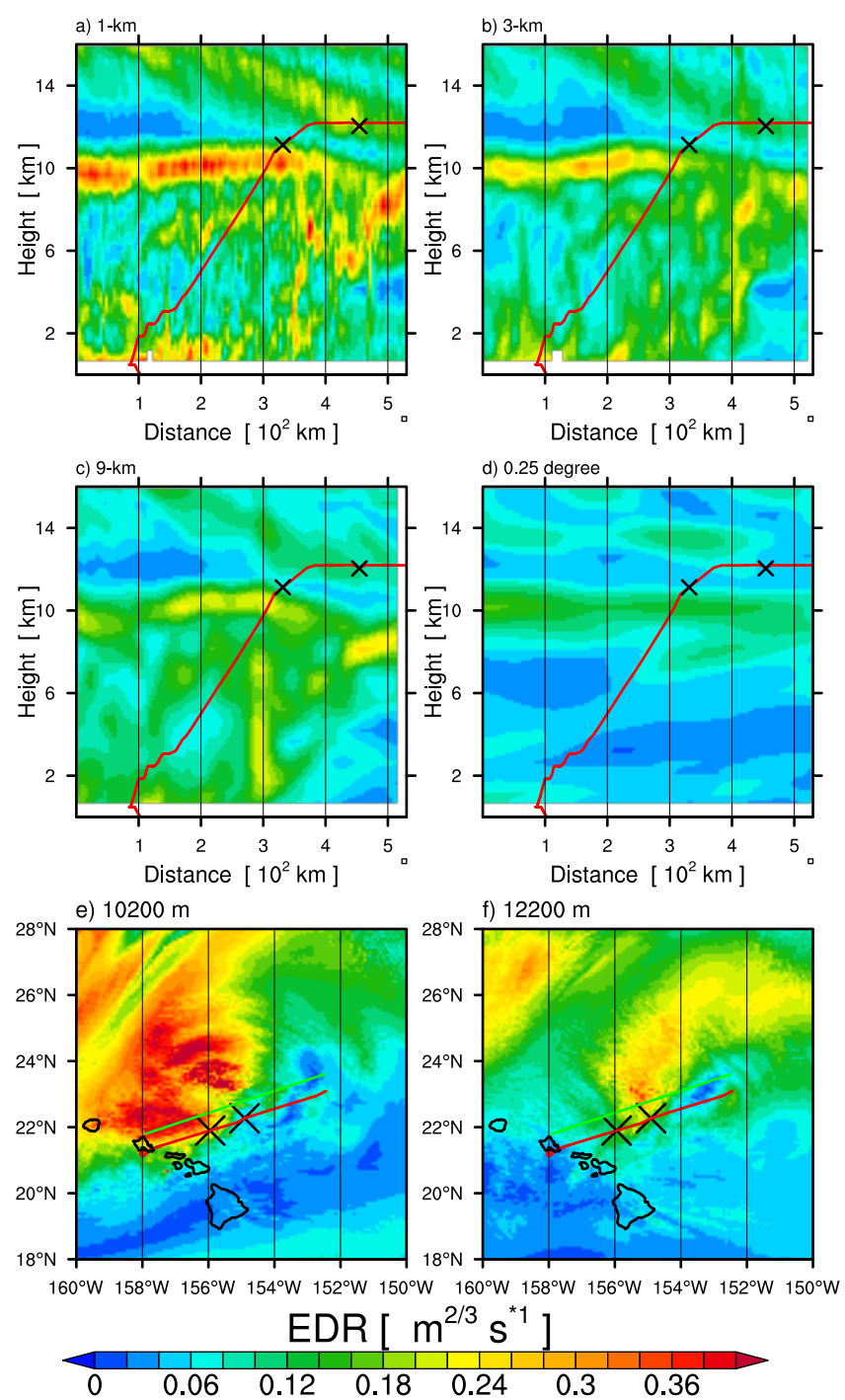
a) 1-km
b) 3-km
c) 9-km
d) 0.25 degree
e) 10200 m
f) 12200 m
Height [km]
Distance [10^2 km]
14
10
6
2
1
2
3
4
5
28°N
26°N
24°N
22°N
20°N
18°N
160°W
158°W
156°W
154°W
152°W
150°W
EDR [m^2/3 s^*1]
0
0.06
0.12
0.18
0.24
0.3
0.36

Figure 3.

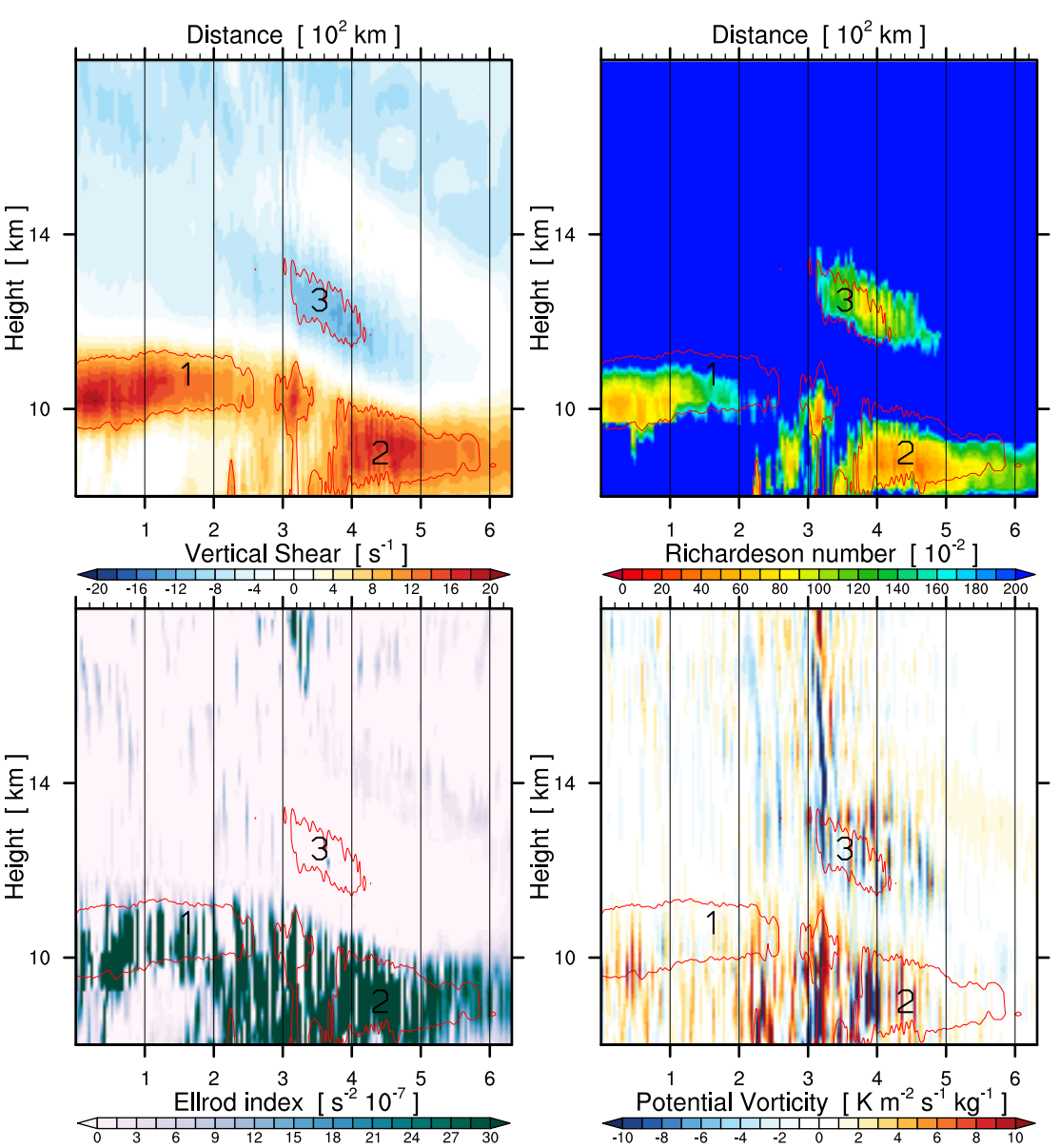
Distance [10^2 km]
Height [km]
14
10
1
2
3
1 2 3 4 5 6
Vertical Shear [s^-1]
-20 -16 -12 -8 -4 0 4 8 12 16 20
Richardeson number [10^-2]
0 20 40 60 80 100 120 140 160 180 200
Ellrod index [s^-2 10^-7]
0 3 6 9 12 15 18 21 24 27 30
Potential Vorticity [K m^-2 s^-1 kg^-1]
-10 -8 -6 -4 -2 0 2 4 6 8 10

Figure 4.

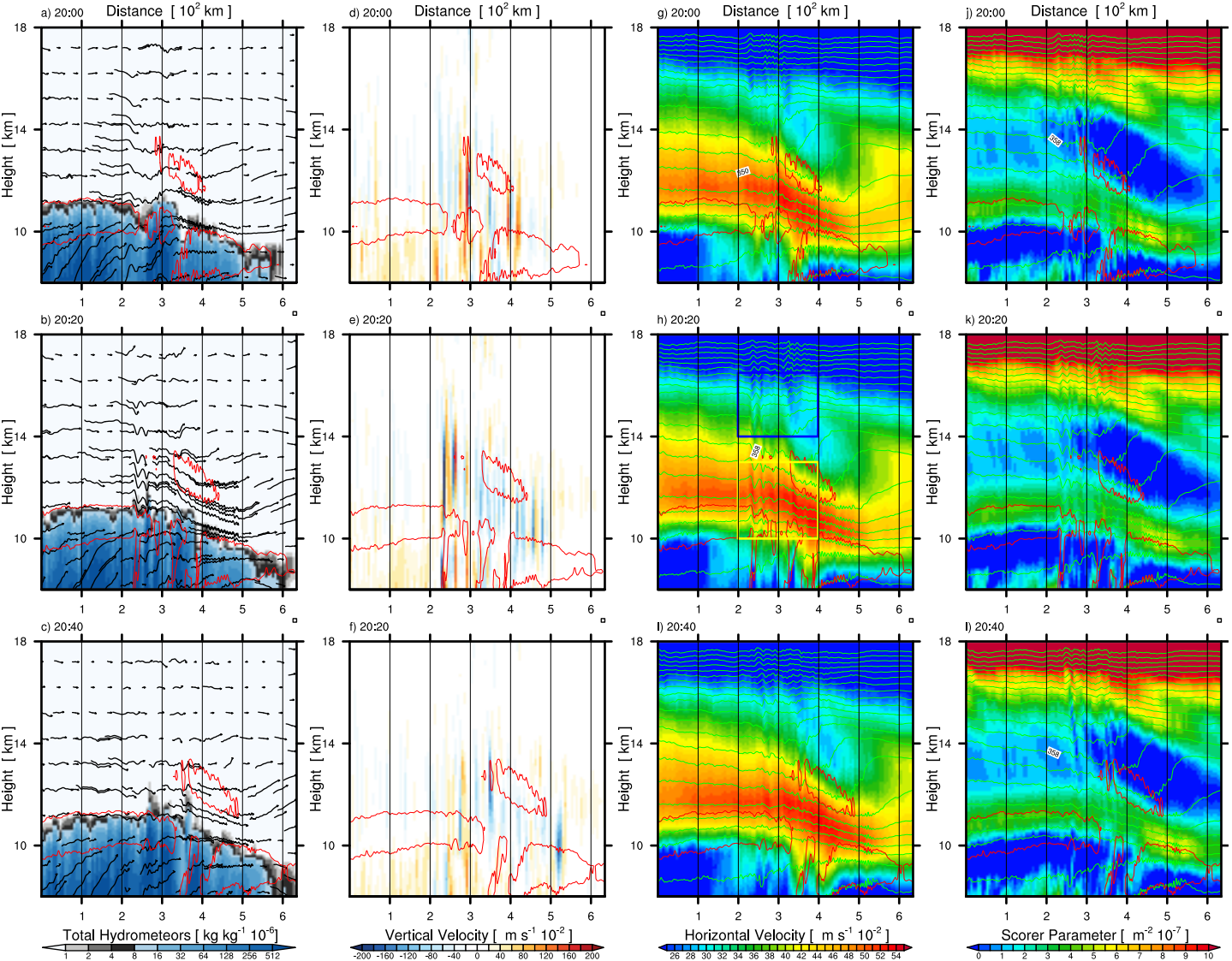
a) 20:00
Distance [10^2 km]
d) 20:00
Distance [10^2 km]
g) 20:00
Distance [10^2 km]
j) 20:00
Distance [10^2 km]
b) 20:20
e) 20:20
h) 20:20
k) 20:20
c) 20:40
f) 20:20
i) 20:40
l) 20:40
Height [km]
18
14
10
1
2
3
4
5
6
Total Hydrometeors [kg kg-1 10-6]
1 2 4 8 16 32 64 128 256 512
Vertical Velocity [m s-1 10-2]
-200 -160 -120 -80 -40 0 40 80 120 160 200
Horizontal Velocity [m s-1 10-2]
26 28 30 32 34 36 38 40 42 44 46 48 50 52 54
Scorer Parameter [m-2 10-7]
0 1 2 3 4 5 6 7 8 9 10